Biomimetic Intelligence and Robotics 4 (2024) 100192

Contents lists available at ScienceDirect

Biomimetic Intelligence and Robotics

journal homepage: www.elsevier.com/locate/birob

Research Article

Modeling and precise tracking control of spatial bending pneumatic soft actuators

Yize Ma, Qingxiang Wu *, Zehao Qiu, Yongchun Fang, Ning Sun

Institute of Robotics and Automatic Information Systems (IRAIS), College of Artificial Intelligence, Nankai University, Tianjin 300350, China
Institute of Intelligence Technology and Robotic Systems, Shenzhen Research Institute of Nankai University, Shenzhen 518083, China

ARTICLE INFO

Article history:
Received 25 July 2024
Revised 2 October 2024
Accepted 22 October 2024
Available online 4 November 2024

Keywords:
Spatial bending
Hysteresis compensation
Prandtl–Ishlinskii modeling
Adaptive feedback control

ABSTRACT

In recent years, a variety of pneumatic soft actuators (PSAs) have been proposed due to the development of soft robots in biomimetic robots, medical devices, etc. At the same time, the modeling and control of PSAs remains an open question. In this paper, a spatial bending pneumatic soft actuator (SBPSA) modeling method based on the Prandtl–Ishlinskii (PI) model is proposed, and the inverse model is designed to compensate for hysteresis nonlinearity. Furthermore, an adaptive feedback controller combined with a hysteresis compensator is proposed for the precise control and tracking of SBPSAs. Finally, an experimental platform is built, and experimental results demonstrate the effectiveness of the proposed method for precise tracking.

1. Introduction

Due to lightweight and flexible materials, soft robots have more advantages in carrying, interacting, and adapting, which leads to an evident development. Therefore, soft robots have shown better advantages in many tasks and scenarios. Compared with rigid robots that are only directly driven by motors, soft robots can adopt various driving methods based on different design structures and flexible materials including liquids [1,2], tendons [3], magnetism [4], and even light [5]. Among them, the pneumatic structures stand out due to their straightforward implementation and emission-free operation. Pneumatic soft actuators (PSAs) are utilized in many robots to interact more gently with humans and the environment, such as soft grippers [6], crawling robots [7], and rehabilitation gloves [8]. Furthermore, considering complex movements of different dimensions, some PSAs are specially designed. In [9], the normal vectors of the two extended layers are opposite to each other. In [10], the bending directions are designed to be perpendicular to each other to achieve motion in three-dimensional space.

According to designs mentioned above, the movements of PSAs can be achieved by a single input air pressure. However, except for flexibility, the difficulties of PSA modeling and control cannot be neglected [11]. Finite element modeling is an effective way to solve modeling problems [12], however, the huge computational cost limits the control application. Neural networks have also achieved certain results in establishing surrogate models [13], however, complex networks make it more difficult to obtain the intrinsic characteristics of actuators from large amounts of data. Although some studies have obtained the dynamic characteristics of soft actuators through basic data-driven methods, the motion of PSAs is more limited to one plane [14]. In addition, the hysteresis phenomenon of PSAs is generally ignored, which can lead to unsatisfactory control performance. To solve hysteresis issues, the Prandtl–Ishlinskii (PI) model is widely used due to the direct calculation of the inverse model.

Furthermore, a series of control methods for soft robots and PSAs are proposed, such as linearized controllers [15], and Lyapunov-based controllers [16]. A model predictive neural controller is designed with a focus on overcoming model uncertainties [17], while an energy-based nonlinear controller [18] is also proposed for the errors of the model. In addition, a sliding mode controller has also been applied to the extension and bending control of PSAs [19]. These methods can be applied to nonlinear systems, however, they cannot combine well with prior laws. Therefore, an adaptive feedback controller based on prior laws should be studied.

Considering the current performance of PSAs and controllers of PSAs, these issues merit attention:

(i) Existing modeling of PSAs mainly focuses on the types of motion in one plane. For spatial bending actuators, the corresponding models are relatively complex, making it difficult to apply for precise control.
(ii) The hysteresis phenomenon in the motion process of PSAs is obvious, and PSA models ignoring the hysteresis phenomenon are not accurate enough.

* Corresponding author.
E-mail address: wuqx@nankai.edu.cn (Q. Wu).

https://doi.org/10.1016/j.birob.2024.100192

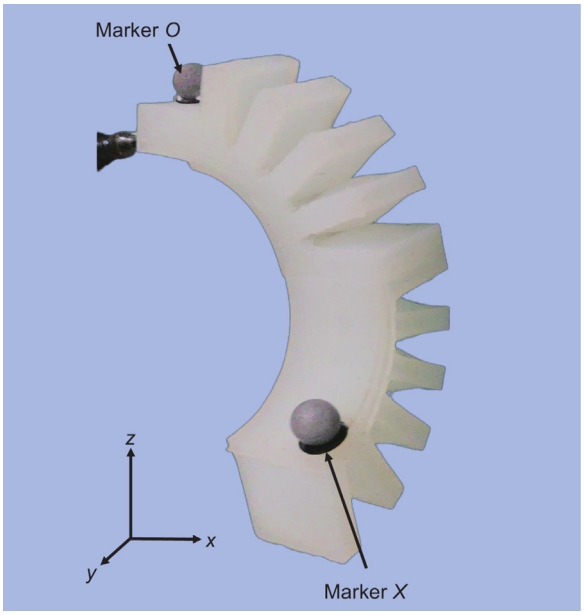

Fig. 1. SBPSA spatial bending effect and measurement target point fixation. The fixed position of SBPSA has a marker point marked as *O*, and its end also has a marker point marked as *X*. These two marker points can be captured by the motion capture system to obtain their positions in the world coordinate system.

(iii) Considering the control design of PSAs, complicated models may lead to higher control costs, and corresponding control algorithms are still immature to realize better performance.

To solve the aforementioned issues, based on a self-made spatial bending pneumatic soft actuator (SBPSA) [20], hysteresis modeling and precise control are realized by original methods. In order to characterize the hysteresis phenomenon of SBPSAs, a PI model is applied and the compensator is designed. Based on the analysis of a large amount of experimental data, the motion of the SBPSA is decomposed into second-order oscillations in different directions. On this basis, an adaptive feedback controller based on decoupling results from different dimensions is designed. With the compensator and controller, SBPSAs can accurately track a predetermined trajectory in each of the three directions.

The remaining structure of the paper is arranged as follows: In Section 2, the hysteresis characteristics of SBPSAs are analyzed, a compensator based on a modified PI model is designed, and an adaptive feedback controller is designed. Several sets of experiments demonstrate the effectiveness of the proposed method in Section 3. Section 4 summarizes the main content of this article.

2. Modeling of SBPSAs and hysteresis compensating

As shown in Fig. 1, SBPSAs are fabricated of silicone, whose two interconnected rapid pneumatic grid units share one air path. With the increase of air pressure, SBPSAs can bend both downward and backward simultaneously. Naturally, the end position of SBPSAs is defined as follows:

$$\boldsymbol{y} = X - O \tag{1}$$

where X represents the three-dimensional coordinates of the end of SBPSAs, and O represents the three-dimensional coordinates of the fixed point of SBPSAs. To obtain the positions of SBPSAs, a marking point is placed at the end of the SBPSA, and a fixed marking point is located at the start.

2.1. Polynomial model of SBPSAs

The 3D motion trajectory of SBPSAs can be decomposed into three independent curves along the three dimensions of the working coordinate system, which can be described by polynomial curves as follows:

$$\boldsymbol{v} = Y(\mu) = \left[\sum_{i=0}^{N_x}\theta_i^x\mu^i \quad \sum_{i=0}^{N_y}\theta_i^y\mu^i \quad \sum_{i=0}^{N_z}\theta_i^z\mu^i\right]^\top \tag{2}$$

where Y represents the three-dimension position of the SBPSA end, θ_i^x, θ_i^y, and θ_i^z represent the weight of the ith term in the x, y, and z dimension separately, μ represents the truly effective atmospheric pressure component, and N_x, N_y, N_z represent the highest order of curves in corresponding dimension, respectively. When the highest degree of Eq. (2) is bigger than 4, $N_{\max} = \max\{N_x, N_y, N_z\} \geq 5$, Y^{-1} cannot be solved analytically. Therefore, numerical search methods can be applied. By treating the model as a series of input–output pairs, the inverse model based on heuristic search is as follows:

$$u = Y^{-1}(\boldsymbol{v}) = S(F\boldsymbol{v}), |F| = 1 \tag{3}$$

where $\boldsymbol{v}$ is the three-dimension position of SBPSA's end, F represents the 3×3 weight matrix, and S represents heuristic search algorithm. It should be noted that the determinant of F must be 1 to ensure that $F\boldsymbol{v}$ is still in the workspace of SBPSAs. At the same time, S includes an interpolation function to ensure that reasonable values can be obtained when its parameters are exactly in the sampling interval.

2.2. Hysteresis model of SBPSAs

To compensate for the hysteresis phenomenon of the SBPSAs, a PI model is adopted in this subsection. Specifically, the hysteresis loops in the PI model are generally expressed as follows:

$$T_\varepsilon[u](k) = \max\{u(k) - \varepsilon, \min\{u(k) + \varepsilon, T_\varepsilon(k-1)\}\}, \varepsilon > 0 \tag{4}$$

where $u(k)$ represents the input at the kth sampling moment, ε is half of the width of delayed death. The hysteresis operator of the PI model can be obtained by weighting the sum of several hysteresis loops, which is expressed as follows:

$$Hp[u](k) = \sum_{i=1}^{N_v}\beta_i T_{\varepsilon_i}[u](k) \tag{5}$$

where N_v represents the number of $T_\varepsilon[u](k)$, β_i is the weight of the ith hysteresis loop, and ε_i represents half the delayed death of the ith hysteresis loop.

The inverse model of PI has the same form as its positive model, which is as follows:

$$Hp^{-1}[\mu](k) = u(k) = \sum_{i=1}^{N_v}\beta_i' T_{\varepsilon_i'}[p](k) \tag{6}$$

where μ represents the output at the kth sampling moment, β' represents the weight of the ith hysteresis loop in the inverse model, and ε_i' represents half of the delayed death of the ith hysteresis loop in the inverse model. Specifically, β' and ε' can be expressed as follows:

$$\begin{cases} \varepsilon_i' & = \sum_{j=1}^{i}\beta_j(\varepsilon_i - \varepsilon_j), (i = 1, 2, 3, \ldots, N_v) \\ \beta_1' & = \dfrac{1}{\beta_1} \\ \beta_i' & = -\dfrac{\beta_i}{\left(\sum_{j=1}^{i}\beta_j\right)\cdot\left(\sum_{j=2}^{i-1}\beta_j\right)}, (i = 2, 3, \ldots, N_v) \end{cases} \tag{7}$$

Due to the difficulty of traditional PI models in handling the asymmetric hysteresis characteristics of soft actuates, it is necessary to modify the PI model. After polynomial correction, the PI model is expressed as follows:

$$H = H_p[\mu](k) + Q(\mu) \tag{8}$$

where $Q(k)$ represents the polynomial. Specifically, $Q(k)$ can be expressed as follows:

$$Q(\mu) = \sum_{i=1}^{N_p} \omega_i \mu^i \tag{9}$$

where N_p represents that the degree of $Q(k)$, and ω_i is the weight of μ^i. Similarly, the inverse model also needs to be modified. Since $Q(k)$ breaks the symmetry of the PI model, the inverse model becomes an implicit function. However, an approximate inverse model can be obtained through the feedback loop, which is expressed as follows:

$$H^{-1} = \frac{Hp^{-1}}{1 + QHp^{-1}} \tag{10}$$

where Hp^{-1} denotes the inverse PI model in Eq. (6), and Q is the polynomial correction term in Eq. (9). Based on the small gain principle, it can be demonstrated that the inverse model in Eq. (10) converges to the implicit function within finite time [21].

2.3. Data-based modeling

Based on the modified PI model, model parameters can be obtained through data-driven methods. Firstly, the identification of Y is important. In order to save computational costs while also considering fitting accuracy, the orders of the polynomial vector are designated as $N_x = N_y = N_z = 5$. Due to the proportional valve's ability return air pressure signals, it is convenient to associate three-dimensional positions with air pressure. Here, the pressure sequence follows a sine function as follows:

$$p(t) = a \times \sin(\pi t / T_0) + a_0 \tag{11}$$

where a is the amplitude, a_0 is the bias to ensure that SBPSAs operate within safe air pressure, t is the time in seconds, π is 3.14, and T_0 is the period. By adjusting the parameters, corresponding data on the three-dimensional positions and pressure at the end of SBPSAs can be obtained, while avoiding the influence of the hysteresis on SBPSAs.

The corresponding relationship between air pressure and three-dimensional positions can be obtained through the feedback signals of the proportional valve and the data of the dynamic capture system. With these input–output pairs, Y^{-1} can be identified through search methods. Specifically, a binary search process that finds the nearest two input–output pairs and a linear interpolation process is executed.

In addition, H in Eq. (8) can be identified by a set of fast-changing sine wave pressures with different frequencies. Different from avoiding delay characteristics when getting Y, getting H needs the hysteresis characteristics of SBPSAs to be fully displayed. Therefore, SBPSA hysteresis characteristics are obtained by the sine wave signal [22] as follows:

$$p(t) = \begin{cases} b_1 \sin\left(\pi \dfrac{t}{T_1}\right), & nT < t \le nT + T_1 \\ b_2 \sin\left(\pi \dfrac{t - T_1}{T_2}\right), & nT + T_1 < t \le (n+1)T - T_3 \\ b_3 \sin\left(\pi \dfrac{t - T_1 - T_2}{T_3}\right), & (n+1)T - T_3 < t \le (n+1)T \end{cases} \tag{12}$$

where T is the period and $T = T_1 + T_2 + T_3$, T_1, T_2, T_3 are the three period, b_1, b_2, b_3 are different amplitudes, and n is the number of periods. The above parameters can be identified using least squares methods.

2.4. Adaptive feedback controller

In order to accurately control SBPSAs and utilize prior experience, an adaptive feedback controller based on a hysteresis compensator is designed. The block diagram of the entire system is shown in Fig. 2. Firstly, the system error is defined as follows:

$$\begin{cases} e_p &= Y^{-1}(\boldsymbol{y}_d) - Y^{-1}(\boldsymbol{y}) \\ e_h &= H^{-1}(e_p) \end{cases} \tag{13}$$

where e_p is the error. Then, a PID controller can be represented as follows:

$$u(t) = K_p(t)e_h(t) + K_i(t)\int_{\tau=0}^{t} e_h(\tau)\mathrm{d}\tau + K_d(t)\frac{\mathrm{d}e_h}{\mathrm{d}t} \tag{14}$$

where $K_p(t)$, $K_i(t)$, and $K_d(t)$ are the parameters of the PID controller and can be adjusted by adaptive feedback control. If $\left[K_p(t), K_i(t), K_d(t)\right]^\top$ is denoted as $\boldsymbol{K}(t)$, it can be expressed as follows:

$$\boldsymbol{K}(t) = \boldsymbol{K}_0 + \hat{\boldsymbol{K}}(t), |\boldsymbol{K}_0| > 0 \tag{15}$$

where $\boldsymbol{K}_0$ represents the basic value, and $\hat{\boldsymbol{K}}(t)$ represents the adjustment value determined by adaptive feedback controller.

The input of the adaptive feedback controller is the compensated error e_h in Eq. (13) and its derivative $\dot{e}_h$, while the output of the adaptive feedback controller is $\hat{\boldsymbol{K}}$. Choose the triangular function as the membership function, which can be expressed as follows:

$$f(x; a, b, c) = \begin{cases} 0, & x \le a \\ \dfrac{x-a}{b-a}, & a < x \le b \\ \dfrac{c-x}{c-b}, & b < x \le c \\ 0, & c \le x \end{cases} \tag{16}$$

where a, b, and c are the parameters that can determine the shape of a triangular function, and x represents the variable whose membership value will be calculated.

In addition, fuzzy rules are presented in Table 1, where EN, EZ, and EP represent the negative, medium, and positive of e, respectively; SN, SZ, and SP represent $\dot{e}$ is negative, medium, and positive, respectively. Meanwhile, p, i, and d represent the membership function of K_p, K_i, and K_d, respectively, and N, Z, and P represent negative, medium, and positive respectively. For ease of understanding, pZ represents that K_p is near the middle, and the same applies to others.

For example, in Table 1, row SN, column EN represents the fuzzy rule as follows:

If $e \in$ EN and $\dot{e} \in$ SN, then $K_p \in$ pP, $K_i \in$ iP, $K_d \in$ dN,

which means when e and $\dot{e}$ are negative, K_p and K_i should be positive and K_d should be negative. All parameters of fuzzy rules and membership function are the parameters of adaptive control methods.

3. Experiments

In order to verify the effectiveness of the proposed method, an experimental environment is set up and several sets of experiments are conducted.

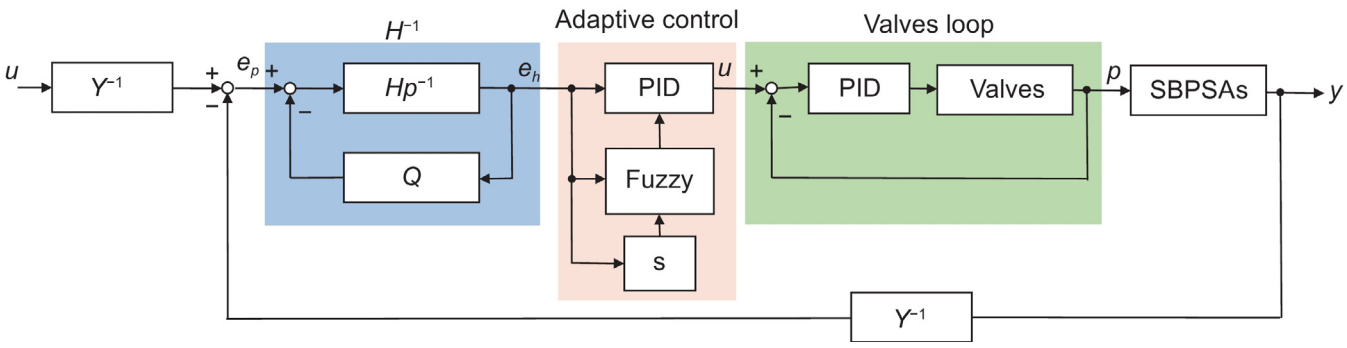

Fig. 2. Control blocks of SBPSAs. Hysteresis compensator (blue block), adaptive controller (pink block), and proportional valve closed loop (green block).

Table 1
Rules of adaptive feedback controllers.

e	$\dot{e}$	K_p	K_i	K_d
EN	SN	pP	iP	dN
	SZ	pN	iP	dZ
	SP	pZ	iP	dN
EZ	SN	pN	iP	dZ
	SZ	pN	iP	dP
	SP	pN	iP	dZ
EP	SN	pZ	iN	dN
	SZ	pZ	iP	dZ
	SP	pP	iP	dZ

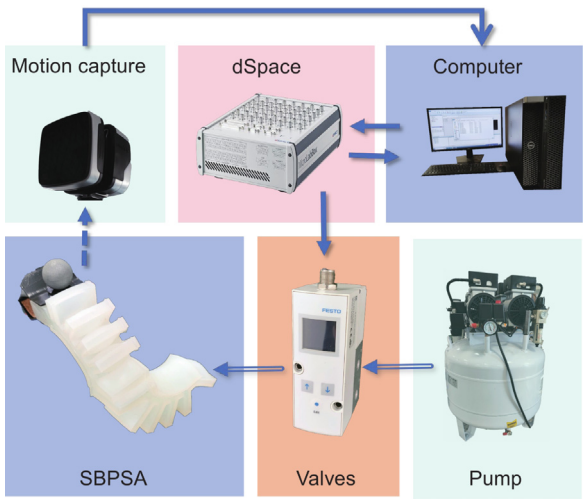

Fig. 3. Experimental conditions and environments of SBPSAs.

The entire system of SBPSAs is shown in Fig. 3. A pump is utilized to provide constant air pressure. Proportional valves change the air pressure. A dSpace is a real-time simulation and experimental platform. A motion capture system can obtain the end position of SBPSAs. A computer is a terminal for operation.

To ensure the rapid and accurate provision of the required air pressure by the proportional valve, the comparative valve adopts a feedback PID controller. In the outer loop control, the controller is divided into four parts: the polynomial compensator, the hysteresis compensator, the adaptive feedback controller, and the inner loop of valves. By inputting the temporal position in three-dimensional space into the computer, the end of the SBPSA will move to a specific position under the adjustment of the compensator and controller.

3.1. Preliminary experiments

First, a set of pressure data is applied to obtain the end workspace of SBPSAs. The safe working pressure of SBPSAs is between 1 and 1.5 bar (1 bar = 0.1 MPa). The input $p(t)$ can be expressed as follows:

$$p(t) = 0.19 + 0.15\sin(\frac{t}{200})\ \text{bar} \tag{17}$$

The three-dimension workspaces can be seen in Fig. 4. It can be seen from Fig. 4 that, the end of SBPSAs can quickly move to the target position with the proposed method.

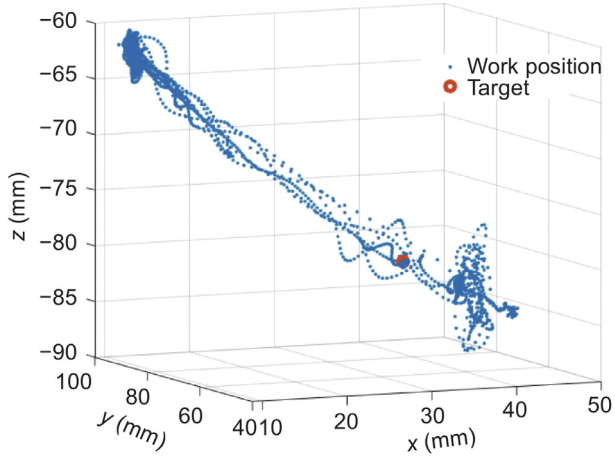

Fig. 4. Workspaces of SBPSAs.

3.2. Accurate control experiments

In this experiment, the end of SBPSAs are controlled to move to a specific position in a workspace. The moving process of the SBPSA end in three directions can be seen in Figs. 5, 6, and 7. The input position A_d is expressed as $A_d = \begin{bmatrix}35.6 & 69.1 & -80.5\end{bmatrix}^\top$, where A_d is the target point in Fig. 4. As can be seen, the PID method, sliding mode controller (SMC), and proposed method can accurately drive the end of SBPSAs to reach the target position, while the open-loop method produces significant steady-state errors. In addition, the proposed method has a better control effect than that of the PID method, mainly reflected in faster response time and shorter adjustment time in three directions. Also, in the initial stage, with a significant error, the gain is set to a larger value for a faster response. After a few seconds, the gain begins to decrease to avoid excessive overshoot.

In addition, Fig. 8 shows the errors of four control methods, including the PID method, open-loop method, SMC, and proposed

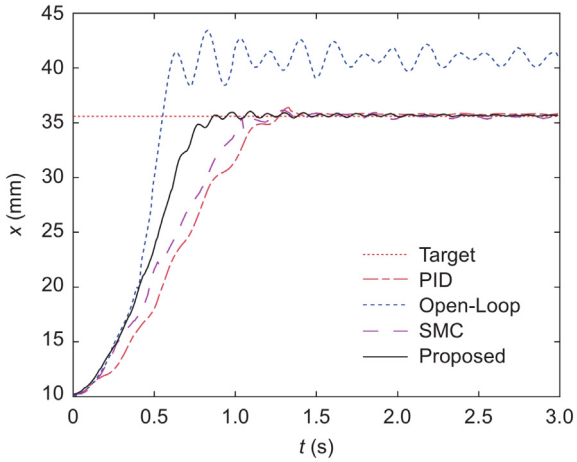

Fig. 5. Experiment 1-*x*. Experimental results of the proposed method (black solid line), open-loop method (blue dotted line), SMC (pink dashed line), and PID method (orange dash-dotted line).

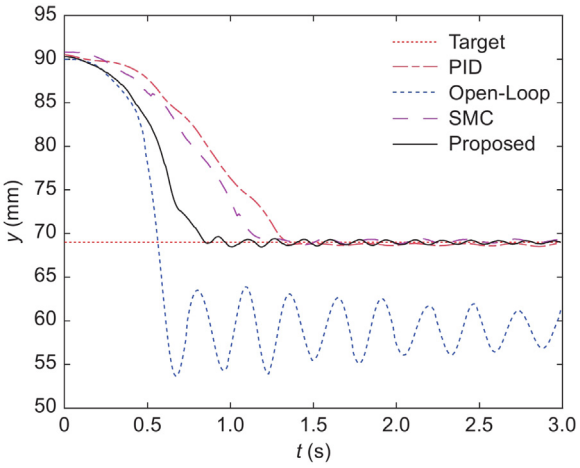

Fig. 6. Experiment 1-*y*. Experimental results of the proposed method (black solid line), open-loop method (blue dotted line), SMC (pink dashed line), and PID method (orange dash-dotted line).

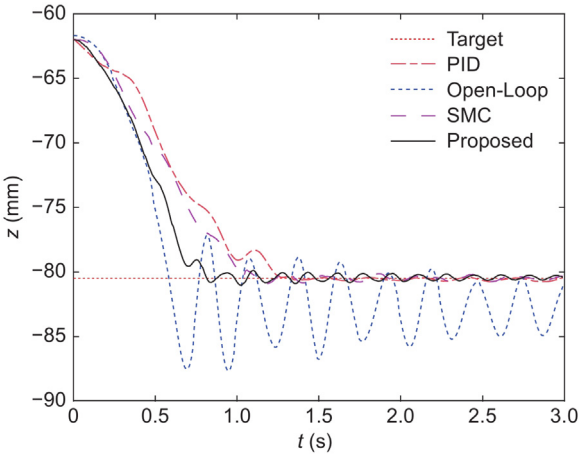

Fig. 7. Experiment 1-*z*. Experimental results of the proposed method (black solid line), open-loop method (blue dotted line), SMC (pink dashed line), and PID method (orange dash-dotted line).

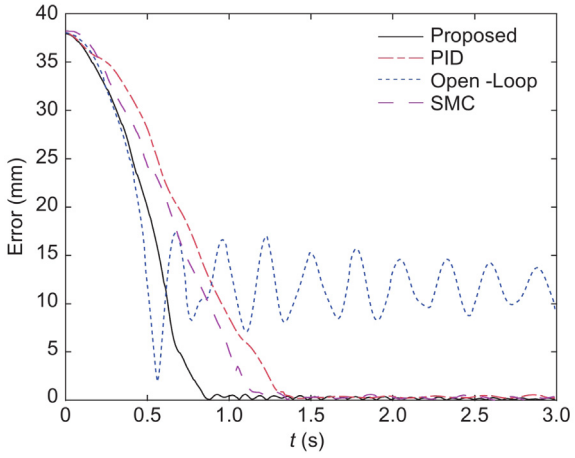

Fig. 8. Experiment 1-*e*. Experimental results of the proposed method (black solid line), open-loop method (blue dotted line), SMC (pink dashed line), and PID method (orange dash-dotted line).

method. The error is specifically the spatial straight-line distance from the marked point X to the target point. Among Figs. 5, 6, and 7, open-loop method has the fastest reaction speed. However, the SBPSA is impacted by the rapid airflow, causing the marked points to deviate from the workspace and thus unable to reach the target position in three-dimensional space throughout the entire bending process of the SBPSA. The proposed method avoids airflow impact, without reducing control efficiency.

3.3. Sine trajectory tracking

This experiment is designed to control the end of SBPSAs to track smooth continuous trajectories in three directions, respectively. The sine wave input is set as the target trajectory for this experiment. By adjusting the F in formula (3), decoupling control in various directions can be achieved. Without considering the motion of other dimensions, the projection of the SBPSA end in one dimension can be controlled, respectively. Several sine waves are used to test the ability of the proposed method, whose input signals $u(t)$ and their corresponding F can be expressed as follows:

Case 1:

$$u(t) = \begin{bmatrix} 8.8\sin(\pi t/5 + 2) + 39 & 0 & 0 \end{bmatrix}^{\top},$$

$$F = \mathrm{diag}[1\ 0\ 0].$$

Case 2:

$$u(t) = \begin{bmatrix} 0 & 15\sin(\pi t/5 - 4) + 58 & 0 \end{bmatrix}^{\top},$$

$$F = \mathrm{diag}[0\ 1\ 0].$$

Case 3:

$$u(t) = \begin{bmatrix} 0 & 0 & 7.1\sin(\pi t/5 + 3) - 66 \end{bmatrix}^{\top},$$

$$F = \mathrm{diag}[0\ 0\ 1].$$

The experimental result can be seen in Figs. 9, 10, and 11. Different control objects being the projection of the SBPSA end in the x-direction, y-direction, and z-direction are tracked, respectively. The target trajectories are selected within an appropriate interval. It can be seen that after the adjustment process of 3 s, the end of SBPSA can accurately track the predetermined trajectories.

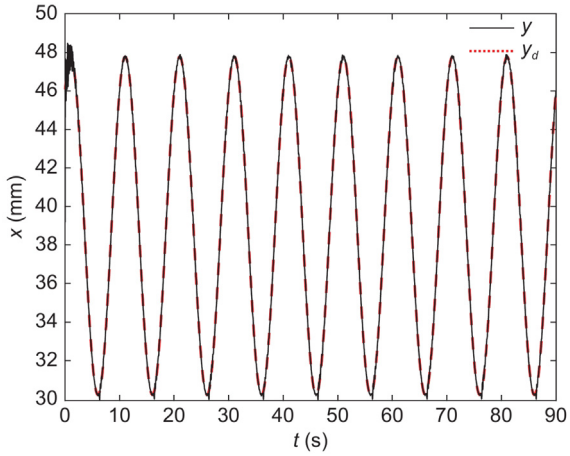

Fig. 9. Experiment 2-Case 1. Experimental results of the proposed method (black solid line).

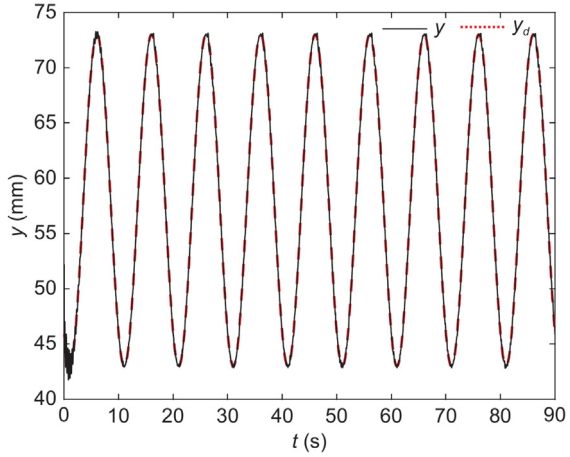

Fig. 10. Experiment 2-Case 2. Experimental results of the proposed method (black solid line).

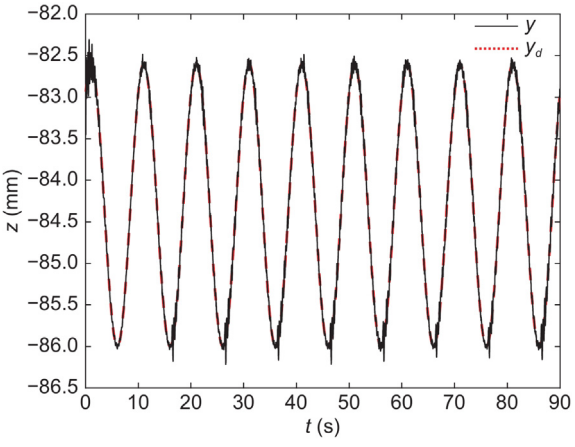

Fig. 11. Experiment 2-Case 3. Experimental results of the proposed method (black solid line).

3.4. Triangle trajectory tracking

To verify the adaptability of the proposed method, a set of triangular wave trajectories is also used in the experiment, and the experimental results can be seen in Figs. 12, 13, and 14. Define the triangular wave function $\Lambda(t; s, a, T)$ as follows:

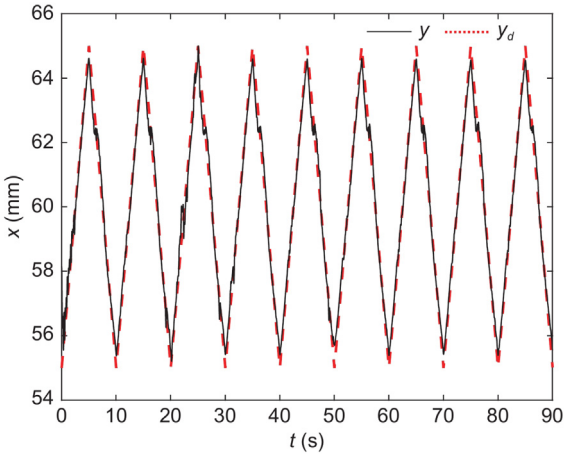

Fig. 12. Experiment 3-Case 1. Experimental results of the proposed method (black solid line).

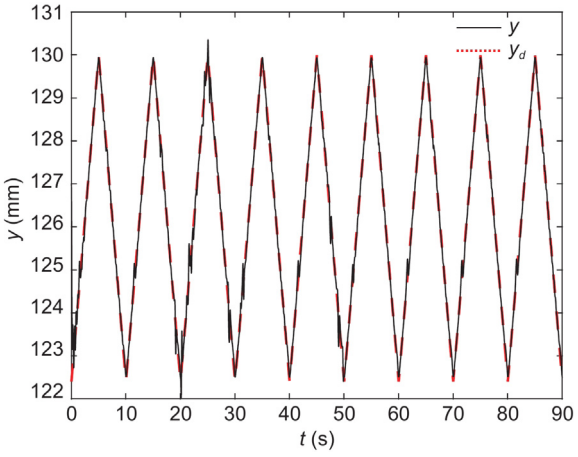

Fig. 13. Experiment 3-Case 2. Experimental results of the proposed method (black solid line).

$$\Lambda(t; s, a, T) = \begin{cases} s + \dfrac{2a}{T}(t - kT), & t \in \left[kT, kT + \dfrac{T}{2}\right) \\ s + 2a - \dfrac{2a}{T}(t - kT), & t \in \left[kT + \dfrac{T}{2}, (k+1)T\right) \end{cases} \tag{18}$$

where s is the bias, a is the amplitude, T is the period, t represents the time, and k represent the kth period, with $k = 0, 1, 2, 3...$ With the definition of triangular waves, the input for the third experiment can be represented as

Case 1:

$$u(t) = \begin{bmatrix} \Lambda(t; 55, 10, 10) & 0 & 0 \end{bmatrix}^\top,$$

$$F = \text{diag}[1\ 0\ 0].$$

Case 2:

$$u(t) = \begin{bmatrix} 0 & \Lambda(t; 122, 8, 10) & 0 \end{bmatrix}^\top,$$

$$F = \text{diag}[0\ 1\ 0].$$

Case 3:

$$u(t) = \begin{bmatrix} 0 & 0 & \Lambda(t; -75, 13, 10) \end{bmatrix}^\top,$$

$$F = \text{diag}[0\ 0\ 1].$$

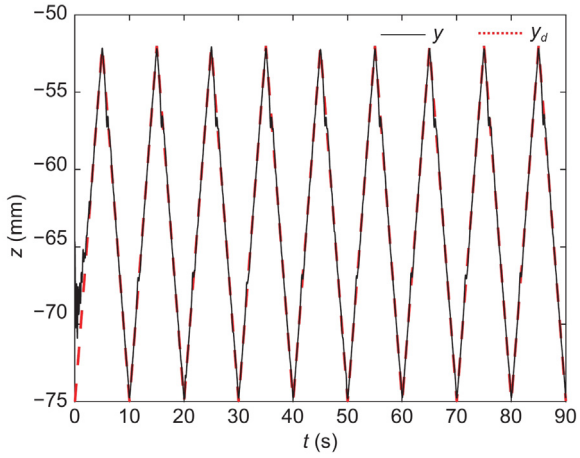

Fig. 14. Experiment 3-Case 3. Experimental results of the proposed method (black solid line).

It can be seen that in all three experiments, SBPSAs can track corresponding trajectories at the end. When the derivative of the target trajectory undergoes sudden changes, SBPSAs can also quickly adjust to reach new target positions, which indicates that the proposed algorithm can track non-smooth trajectories.

4. Conclusion

Based on the PI model, the model of SBPSA has been built. Furthermore, an adaptive control method utilizing a hysteresis compensator has been proposed. Several experiments have demonstrated the effectiveness of the proposed method. Additionally, the proposed method has enabled SBPSAs to reach the target position within 1 s, maintaining a stable error of no more than 1.5 mm projected in the *x*, *y*, or *z* axes. The experimental results have also verified its effectiveness for precise tracking. The proposed method has allowed SBPSAs to accurately track the predetermined trajectory within 3 s, with a tracking error of no more than 4 mm.

CRediT authorship contribution statement

Yize Ma: Writing – original draft. **Qingxiang Wu:** Writing – review & editing. **Zehao Qiu:** Software. **Yongchun Fang:** Supervision. **Ning Sun:** Funding acquisition.

Declaration of competing interest

The authors declare that they have no known competing financial interests or personal relationships that could have appeared to influence the work reported in this paper.

Acknowledgments

This work was supported in part by the National Natural Science Foundation of China (52205019 and 62373198), and in part by the Fundamental Research Funds for the Central Universities (078-63243157).

Appendix A. Supplementary data

Supplementary material related to this article can be found online at https://doi.org/10.1016/j.birob.2024.100192.

References

[1] Y. Feng, T. Ide, H. Nabae, G. Endo, R. Sakurai, S. Ohno, K. Suzumori, Design of a compliant 7-DoF power soft robot driven by hydraulic artificial muscles, in: The 32nd 2021 International Symposium on Micro-Nano Mechatronics and Human Science, 2021, pp. 1–4.
[2] T. Yang, N. Sun, Y. Fang, Adaptive fuzzy control for uncertain mechatronic systems with state estimation and input nonlinearities, IEEE Trans. Ind. Inform. 18 (3) (2021) 1770–1780.
[3] D. Grace, J. Lee-Ortiz, M. Garcia, A. Contreras-Esquen, A. Tekes, A.A.A. Moghadam, Development of a novel six dof soft parallel robot, in: SoutheastCon 2022, 2022, pp. 81–86.
[4] F. Xu, K. Ma, T. Gong, Z. Jiang, C. Hu, Design and testing of a magnetic soft crawling robot with multimodal locomotion driven by 3-D magnetic fields, IEEE Trans. Instrum. Meas. 73 (2024) 1–11.
[5] Y. Peng, P. He, R. Guo, L. Lin, Bioinspired light-driven soft robots by a facile two-mode laser engraving and cutting process, in: 2021 21st International Conference on Solid-State Sensors, Actuators and Microsystems (Transducers), 2021, pp. 10–13.
[6] M.E. Salem, Q. Wang, R. Wen, M. Xiang, Design and characterization of soft pneumatic actuator for universal robot gripper, in: 2018 International Conference on Control and Robots, ICCR, 2018, pp. 6–10.
[7] M. Wu, X. Xu, Q. Zhao, W.H. Afridi, N. Hou, R.H. Afridi, X. Zheng, C. Wang, G. Xie, A fully 3D-printed tortoise-inspired soft robot with terrains-adaptive and amphibious landing capabilities, Adv. Mater. Technol. 7 (12) (2022) 2200536.
[8] P. Polygerinos, S. Lyne, Z. Wang, L.F. Nicolini, B. Mosadegh, G.M. Whitesides, C.J. Walsh, Towards a soft pneumatic glove for hand rehabilitation, in: 2013 IEEE/RSJ International Conference on Intelligent Robots and Systems, 2013, pp. 1512–1517.
[9] S. Nie, X. Liu, H. Ji, Z. Ma, F. Yin, Simulation and experiment study on deformation characteristics of the water hydraulic flexible actuator used for the underwater gripper, IEEE Access 8 (2020) 191447–191459.
[10] Z. Qiu, Q. Wu, Z. Liu, T. Yang, N. Sun, A crocodile-like pneumatic soft crawling robot with three-dimensional deformation actuators, in: 2023 42nd Chinese Control Conference, CCC, 2023, pp. 1–6.
[11] N. Sun, D. Liang, Y. Wu, Y. Chen, Y. Qin, Y. Fang, Adaptive control for pneumatic artificial muscle systems with parametric uncertainties and unidirectional input constraints, IEEE Trans. Ind. Inform. 16 (2) (2020) 969–979.
[12] G. Zheng, O. Goury, M. Thieffry, A. Kruszewski, C. Duriez, Controllability pre-verification of silicone soft robots based on finite-element method, in: 2019 International Conference on Robotics and Automation, ICRA, 2019, pp. 7395–7400.
[13] P. Hyatt, D. Wingate, M.D. Killpack, Model-based control of soft actuators using learned non-linear discrete-time models, Front. Robot. AI 6 (2019) 22.
[14] L. Shi, C. Mucchiani, K. Karydis, Online modeling and control of soft multi-fingered grippers via koopman operator theory, in: 2022 IEEE 18th International Conference on Automation Science and Engineering, CASE, 2022, pp. 1946–1952.
[15] F. Campisano, S. Caló, A.A. Remirez, J.H. Chandler, K.L. Obstein, R.J. Webster III, P. Valdastri, Closed-loop control of soft continuum manipulators under tip follower actuation, Int. J. Robot. Res. 40 (6–7) (2021) 923–938.
[16] F. Xu, H. Wang, W. Chen, Y. Miao, Visual servoing of a cable-driven soft robot manipulator with shape feature, IEEE Robot. Autom. Lett. 6 (3) (2021) 4281–4288.
[17] C. Luo, K. Wang, G. Li, S. Yin, L. Yu, E. Yang, Development of active soft robotic manipulators for stable grasping under slippery conditions, IEEE Access 7 (2019) 97604–97613.
[18] D. Liang, N. Sun, Y. Wu, Y. Chen, Y. Fang, L. Liu, Energy-based motion control for pneumatic artificial muscle actuated robots with experiments, IEEE Trans. Ind. Electron. 69 (7) (2022) 7295–7306.
[19] S. Ibrahim, J.C. Krause, A. Raatz, Linear and nonlinear low level control of a soft pneumatic actuator, in: 2019 2nd IEEE International Conference on Soft Robotics, RoboSoft, 2019, pp. 434–440.
[20] Z. Qiu, Q. Wu, Z. Liu, Y. Fang, N. Sun, A new three-dimensional deformation pneumatic soft actuator with mutually vertical PneuNets, IEEE Trans. Ind. Electron. (2024) 1–10.
[21] Z. Sun, B. Song, N. Xi, R. Yang, L. Hao, Y. Yang, L. Chen, Asymmetric hysteresis modeling and compensation approach for nanomanipulation system motion control considering working-range effect, IEEE Trans. Ind. Electron. 64 (7) (2017) 5513–5523.
[22] P. Huang, J. Wu, P. Zhang, Y. Wang, C.-Y. Su, Dynamic modeling and tracking control for dielectric elastomer actuator with a model predictive controller, IEEE Trans. Ind. Electron. 69 (2) (2021) 1819–1828.